



Quantitative microstructure characterization of a Ni–YSZ bi-layer coupled with simulated electrode polarisation



F. Usseglio-Viretta ^a, J. Laurencin ^{a,*}, G. Delette ^a, J. Villanova ^b, P. Cloetens ^b, D. Leguillon ^c

^a CEA, LITEN, F-38054 Grenoble, France

^b ESRF, 6 rue Jules Horowitz BP 220, 38043 Grenoble, France

^c IJRA, CNRS UMR7190, Université Pierre et Marie Curie, 4 place Jussieu, 75005 Paris, France

HIGHLIGHTS

- Microstructure of a bi-layer Ni–YSZ cermet is analysed from 3D reconstructions.
- Functional layer and substrate are quantified with statistically representative volumes.
- Microstructure properties of all phases are determined for the Ni–YSZ bi-layer.
- Extent of the electrochemical reaction in the support is discussed.
- Electrode activation energy is computed as function of microstructure characteristics.

ARTICLE INFO

Article history:

Received 19 December 2013

Accepted 14 January 2014

Available online 31 January 2014

Keywords:

Ni–YSZ cermet

Microstructure

Electrode polarization

Activation energy

SOEC

ABSTRACT

Microstructure of a cermet Ni–YSZ bi-layer is analysed on the basis of three dimensional reconstructions obtained on both functional layer and cell support. Microstructural parameters of gas, ionic and electronic phases are determined in terms of phase connectivity, mean particles diameter, particles size distribution, specific surface area, tortuosity factor and density of TPBs. Microstructural properties are introduced in an SOEC cathode micro model that takes into account the specific configuration of the Ni–YSZ composite bi-layer. Simulations show that the extent of the electrochemical reaction in the support is very limited. Moreover, it is found that electrode apparent activation energy is a combination of effective ionic conduction and charge transfer in the active functional layer.

© 2014 Elsevier B.V. All rights reserved.

1. Introduction

Because of its great potential, hydrogen production by High Temperature Steam Electrolysis (HTSE) has received an increasing interest in recent years. Hydrogen produced by water electrolysis taking advantage of sustainable energy sources will allow limiting greenhouse gas emission. However, this scheme will be achievable only if the efficiency, durability and reliability of the electrolyser are improved.

The active parts of an electrolyser correspond to a stack of elementary cells, named Solid Oxide Electrolysis Cells (SOECs). SOECs are constituted of a three-layered structure made of ceramic materials: one dense electrolyte of Yttria Stabilized Zirconia (YSZ) is sandwiched between two porous electrodes. The cathode material

is usually a composite of Nickel and YSZ (Ni–YSZ). The Cathode Supported Cell (CSC) configuration is composed of a thick highly porous Ni–YSZ substrate on which a thin electrolyte and the functional electrodes are layered. This geometry has been designed to improve the cell electrochemical efficiency by limiting the ionic losses in the thin electrolyte. Nowadays, the planar CSC geometry allows achieving the best electrochemical performance at usual SOEC operating temperatures (≈ 800 °C) [1–3] and is generally employed in stack preindustrial demonstrators [2–4].

In CSC configuration, the cathode substrate exhibits a coarse microstructure which is crucial for the gas transportation. Indeed, the thick substrate can potentially hinder the gas diffusion and can induce high concentration overpotential at high current density [5–7]. Conversely, the functional layer presents a thinner microstructure which must be optimized to facilitate the electrochemical process and minimize the activation overpotential. For this purpose, the density of Triple-Phase Boundary lengths (TPBs) should be increased as far as possible since it corresponds to the active

* Corresponding author. Tel.: +33 (0) 438782210; fax: +33 (0) 438784139.
E-mail address: jerome.laurencin@cea.fr (J. Laurencin).

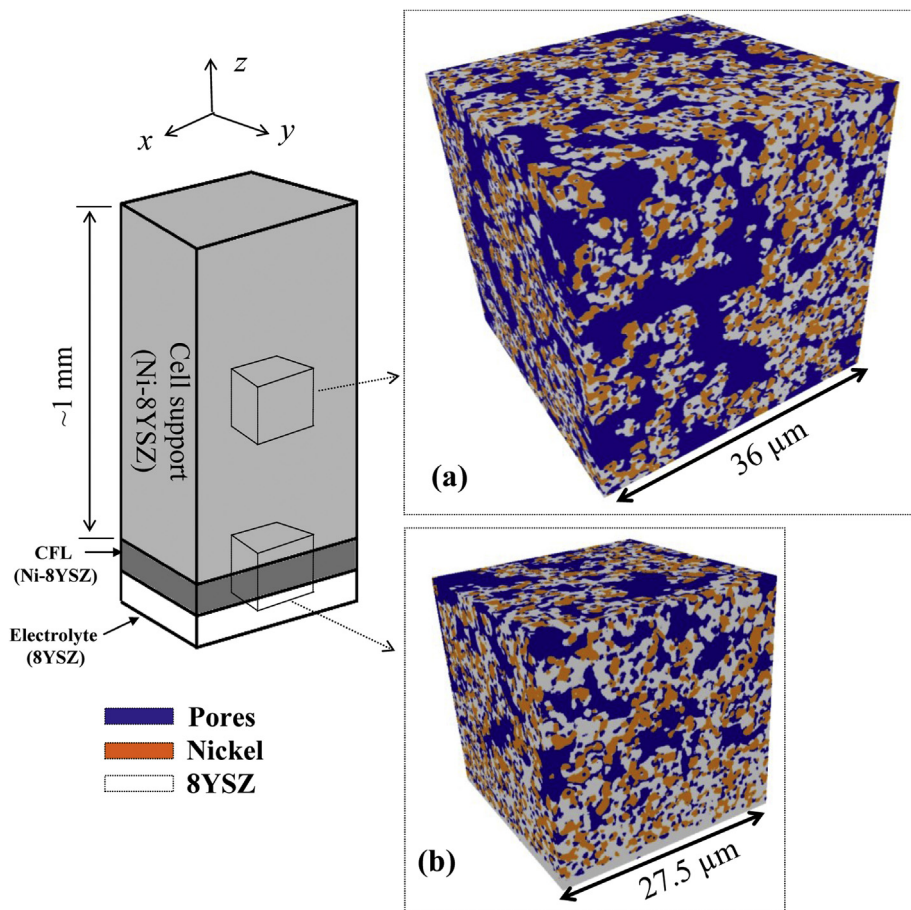


Fig. 1. Three dimensional rendering volumes of studied Ni–YSZ cermet: (a) reconstruction of $36 \times 36 \times 36 \mu\text{m}^3$ taken in the middle of the cell support. (b) Reconstruction of $27.5 \times 27.5 \times 27.5 \mu\text{m}^3$ including the functional layer, a part of the cell support and a part of the electrolyte.

sites where the electrochemical reactions take place [8]. In addition, microstructure of the functional layer must be tailored to promote the effective ionic conduction of the YSZ structure. This requirement implies to lower the YSZ tortuosity factor so that the oxygen ions conductivity is enhanced in the functional layer. Indeed, it has been shown that this parameter governs the extent of the electrochemical reaction from the electrolyte interface within the functional layer [8].

Therefore, microstructure properties of both functional layer and substrate have to be quantified precisely and correlation with electrode polarisation must be established. For this purpose, there is a strong interest to use micro models able to analyse the impact of electrode microstructure properties on activation and concentration overpotentials. In a previous paper [8], the authors established such an electrochemical micro model and performed parametric studies to evaluate some degradation mechanisms.

In this paper, it is proposed to compute the microstructure features of a typical CSC Ni–YSZ electrode from three dimensional reconstructions obtained by X-ray nano-tomography [9]. Both functional layer and support are analysed and the microstructure properties of gas, ionic and electronic phases are determined for the two layers. For the first time, the main microstructural characteristics of a Ni–YSZ cermet bi-layer are quantified with a large field of view ($\approx 50 \mu\text{m}$), in terms of (i) tortuosity factors of each phase, (ii) density of TPBs, (iii) Particles Size Distribution (PSD) and (iv) mean particles diameters. The local in-house micro-model [8] is then used to relate the microstructure properties to the electrode polarization. Impact of the microstructure on the global electrode

response is analysed. In this frame, a special attention has been paid to estimate the possible electrochemical activity of the Ni–YSZ substrate. For this purpose, the extent of the electrochemical reaction from the functional layer into the support is calculated as a function of its real microstructure properties. The extraction of the electrode exchange density as a function of temperature is also addressed in this article. It is shown that the combination of ionic conduction and charge transfer all along the volume results in an apparent activation energy or the electrode activation consistent with the published experimental data.

2. Material and methods

2.1. Sample and X-ray nano-tomography characterisation

Sample investigated in the present work was taken from commercial CSC supplied by the Forschungszentrum Jülich (FZJ) research centre [10]. Cathode is constituted by a bi-layer made of 50 wt% Ni and 50 wt% 8YSZ (ZrO_2 stabilised with 8 mol% Y_2O_3). It includes a thin Cathode Functional Layer (CFL) deposited onto a thick Cathode Current collector (CCC). The CCC substrate is $\approx 1 \text{ mm}$ thick and is used as the cell structural support. The CFL and the 8YSZ electrolyte are co-sintered with the cell support and present a thickness of $\approx 10 \mu\text{m}$.

Synchrotron X-ray nano-tomography experiments have been carried out at the European Synchrotron Radiation Facility (ESRF beam line ID22) to characterize the three dimensional structure of CFL and CCC layers. The tomography procedure is based on an

optical phase contrast imaging technique that follows a holotomographic scheme [11]. The method is well adapted to separate the porosity [12] as well as the different solid phases having the same X-ray absorption such as Ni and YSZ [9]. The 3D reconstructions present a large field of view ($\approx 50 \mu\text{m}$) with a voxel size of 25 nm. Further details on data acquisition, algorithm for 3D reconstructions and image segmentation are reported in Villanova et al. [9]. The reconstructed volume of the studied CFL and CCC layers is also provided in Ref. [9]. Fig. 1a and b illustrates 3D rendering volumes related to the Ni–YSZ support and functional layers. It can be noticed that these volumes are sufficiently large to be statistically representative for the studied heterogeneous media. Indeed, the Representative Volume Elements (RVEs) are roughly equal to $35 \times 35 \times 35 \mu\text{m}^3$ [12] and $13 \times 13 \times 13 \mu\text{m}^3$ [9] for the current collector and functional layer respectively.

2.2. Procedures for microstructures quantification

A set of programs has been implemented in Matlab[®] software to compute all the microstructural properties required for the electrode modelling. Methods and algorithms to determine the volume fraction, phase connectivity and “apparent” tortuosity factors have been already presented in Laurencin et al. [12]. A short abstract is given hereafter while methods for determining surface specific area, mean particle diameter, particle size distribution and length of TPBs are described more precisely.

2.2.1. Phase connectivity

For determining the phase contiguity, it is reminded that two cubic voxels of the reconstruction are assumed to be connected only if they share a common face. Inversely, two neighbouring cubic voxels are supposed to be disconnected if they are only linked by an edge or a vertex.

2.2.2. Tortuosity factor

The “apparent” tortuosity factors of gas, ionic and electronic conducting phases are determined by using a homogenization technique. For this purpose, each phase of the reconstructed domain is converted into an independent finite element mesh. The diffusional flow is then computed for each phase as a function of its bulk gas diffusivity $D_{\text{gas}}^{\text{bulk}}$ or electrical conductivities σ_i^{bulk} (i.e. $D_{\text{gas}}^{\text{bulk}}$ is equal to the gas diffusivity and σ_i^{bulk} is related to electronic or ionic conductivities). In practice, simulations are carried out with zero flux condition at the phase interface within the domain. An intermediate boundary condition is applied onto the two opposite faces along the studied direction of the simulated volume. One concentration is imposed upon the first face whereas the opposite one undergoes an imposed flux. The effective diffusion coefficient $D_{\text{gas}}^{\text{eff}}$ (or the effective conductivity σ_i^{eff}) is then deduced from the numerical analysis by equating the macro homogeneous flux to the average value computed from the simulation. The “apparent” tortuosity factor τ is then given by the following relation [13]:

$$D_{\text{gas}}^{\text{eff}} = \frac{\varepsilon_{\text{gas}} D_{\text{gas}}^{\text{bulk}}}{\tau_{\text{gas}}} \text{ and } \sigma_i^{\text{eff}} = \frac{\varepsilon_i \sigma_i^{\text{bulk}}}{\tau_i} \quad (i = \text{ionic or electronic phase}) \quad (1)$$

where ε represents the volume fraction of the analysed connected phase. It can be mentioned that such definition of the tortuosity factor encompasses two distinct contributions. The first one is related to a pure “geometrical” tortuosity. It takes into account the fact that flow is hampered since the pathways for diffusion are not straight but sinuous and intricate. The second contribution is caused by some flux constriction effects in the microstructure since cross section areas for diffusion are not constant [14–16].

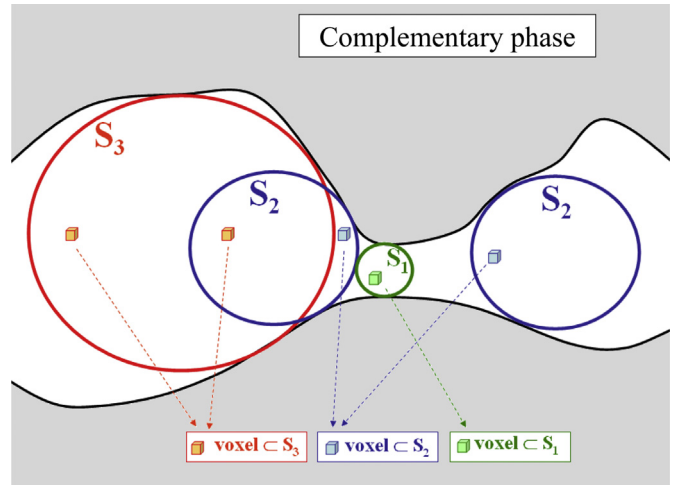


Fig. 2. Schematic representation of the analysed phase for PSD calculation. The volume is covered by a set of overlapping spheres (which must be tangential to the complementary phase). The voxels are attributed to the largest sphere.

2.2.3. Mean particle diameter and surface specific area

The mean particle diameter and surface specific area can be computed from basic morphological tools [17,18]. The geometrical covariogram $K(h)$ can be presented as a measure of the intersection between the phase and its image after a translation h of the medium. Considering the x -direction, $K(h)$ is expressed as followed:

$$K(h) = \iiint_{V(h)} k(x, y, z) \times k((x+h), y, z) \times dV \text{ and} \\ k(x, y, z) = \begin{cases} 1 & \text{if } (x, y, z) \text{ belongs to the studied phase} \\ 0 & \text{if } (x, y, z) \text{ is not included in the studied phase} \end{cases} \quad (2)$$

where $V(h)$ is the intersection volume. The differentiation of $K(h)$ when $h = 0$ provides an exact determination of the specific surface area, S_p [17,18]:

$$S_p = \frac{S_{\text{area}}}{V_{\text{phase}}} \quad \text{with } S_{\text{area}} = -4 \times \frac{d(K(h))}{dh} \Big|_{h=0} \quad (3)$$

Such a method offers the advantage to be independent of the reconstructed phase digitalization in cubic voxels, while a direct computation of S_p is overestimated and depends of the voxelization [12].

The covariance function $C(h)$ can be used to determine the mean phase diameter \bar{d} . The function represents the probability that 2 points of the domain separated by a distance h are included in the same phase:

$$C(h) = P\{x \in \text{phase}, x+h \in \text{phase}\} = \frac{1}{N} \sum_{i=1}^{i=N} k(x, y, z) \times k((x+h), y, z) \quad (4)$$

where N is the number of realizations (i.e. for each distance h , N corresponds to the number of position x where the relation $k(x, y, z) \times k((x+h), y, z)$ is calculated). It can be noticed that this 2 points probability function $C(h)$ can be related to the geometrical covariogram $K(h)$ according to $C(h) = K(h)/V(h)$. This function tends to an asymptotic limit at a distance of correlation h^* . It means that the 2 points k and $k(h)$ are not correlated anymore. The length h^* corresponds to a characteristic dimension of the medium [17,19] which can be ascribed to the mean particle diameter (i.e. $h^* = \bar{d}$).

2.2.4. Particle size distribution

Several methods can be employed to determine the particle size distribution [20,21]. In the present work, a pure geometrical approach has been adopted [20]. As illustrated in Fig. 2, the analysed phase is represented by a set of overlapping spheres, each one being tangent to the complementary phase. The term $p(r_i)$ is then defined as the probability that a voxel belongs to the largest sphere S of radius r_i . In order to compute this probability, voxels belonging to the spheres $S(r_i)$ are identified and their volumes are added together (Fig. 2). The resulting sum is normalized by the phase volume:

$$p(r_i) = \frac{1}{V_{\text{phase}}} \sum_{V_{\text{voxel}}} f \times V_{\text{voxel}}(x, y, z) \quad \text{with } f = \begin{cases} 1 & \text{if } (x, y, z) \subset S(r_i) \\ 0 & \text{if } (x, y, z) \not\subset S(r_i) \end{cases} \quad (5)$$

With V_{voxel} denotes the voxel volume located in (x, y, z) coordinate. The cumulative probability, representing the probability P that a voxel belongs to a sphere of radius equal or inferior to R , can be deduced from eq. (5):

$$P(0 \leq r \leq r_n = R) = \sum_{i=1}^{i=n} p(r_i) = \int_0^R \text{PSD}(r) dr \quad (6)$$

where the Particle Size Distribution (PSD) corresponds to the density probability function. This description provides an exact distribution for cylinder or spherical morphology. Nevertheless it has been shown that it remains suitable for irregular medium [20] such as the studied materials.

2.2.5. Triple phase boundary lengths

The total length of TPBs is calculated by counting all the voxel edges in contact with elements belonging to gas, ionic and electronic phases. The numerical procedure implemented in Matlab® is the same that the one described in Vivet et al. [22]. The computation is performed according to the three directions x , y and z of the reconstruction. For each direction (x , y or z -direction), all the voxel edges included in the perpendicular plane (yz , xz or xy -plane) are inspected. If they are identified as TPB segments, their lengths are added to the total length of TPB. However, such a determination leads to an over estimation since the oblique TPB line in the reconstruction is constituted of orthogonal segments. To take into account this shortcoming, the corrective factor proposed by Wilson et al. [23] is applied by dividing the raw value of TPB length by 1.455. This calculated value is referred as the total TPB length since it is computed from the whole phases of the reconstructed volume. The electrochemical active length of TPB is obtained by restricting the same numerical procedure to the connected phases.

2.3. Electrode model description

The structural properties computed from the 3D reconstructions are introduced in an in-house electrode modelling implemented in Matlab®. The model has been already detailed in a previous article [8]. A brief summary is given here by highlighting some modifications. Indeed, the model has been adapted in order to take into account the electrode configuration made of a Ni–YSZ composite bi-layer (i.e. a functional layer layered on a thick substrate in which the electrochemical reaction can potential extend).

The model is isothermal and considers one slice of electrode embedding the functional layer and the cell support (Fig. 3). Within

the functional layer, the electrons and ions fluxes are calculated according to Ohm's law into the electronic and ionic conducting phases (cf. coordinate system depicted in Fig. 3):

$$i_{\text{io}}(z) = -\sigma_{\text{io}}^{\text{eff}} \times \frac{d\varphi_{\text{io}}}{dz} \quad \text{and} \quad i_{\text{e}^-}(z) = -\sigma_{\text{e}^-}^{\text{eff}} \times \frac{d\varphi_{\text{e}^-}}{dz} \quad (7)$$

where i_{io} and i_{e^-} are the local electronic and ionic current densities calculated in the Ni and YSZ materials respectively. The terms, φ_{io} and φ_{e^-} are related to the electronic and ionic potential picked up in the electronic and ionic conducting phase. The effective conductivities are expressed according to eq. (1) as a function of the 'apparent' tortuosity factor and the volume fraction of each phase. The bulk conductivity of the ionic 8YSZ phase is thermally activated and follows an Arrhenius law ($\sigma_{\text{io}=8\text{YSZ}} (\text{S cm}^{-1}) = 466 \exp(-82,616/(RT))$ with temperature T in K [8,24]). Mass transfer of gas through the connected porosity is calculated in the frame of the Dusty Gas Model (DGM) than combines molecular and Knudsen diffusion. The effective gas diffusivities are still calculated by multiplying the bulk coefficients by the ratio of the connected porosity to the gas tortuosity factor. Moreover, it can be mentioned that the Knudsen coefficient depends on the mean pores diameter. In the model, it is assumed that the electrochemical reactions can potentially occur in the whole functional layer at the active TPBs. The rates of the electrochemical reaction $v(z)$ are computed from a Butler–Volmer formalism considering a single charge transfer. The kinetic depends on the local partial pressure of hydrogen and steam, $P_{\text{H}_2}(z)$ and $P_{\text{H}_2\text{O}}(z)$, computed in the thickness of the layer:

$$v(z) = \left\{ k_{\text{ox}} e^{\frac{\alpha_{\text{ox}} 2FE(z)}{RT}} P_{\text{H}_2}(z) - k_{\text{red}} e^{\frac{-\alpha_{\text{red}} 2FE(z)}{RT}} P_{\text{H}_2\text{O}}(z) \right\} \quad (8)$$

where R and F denote the gas constant and Faraday's constant. Coefficients α_{ox} and α_{red} correspond to symmetry factors of the reaction ($\alpha_{\text{ox}} + \alpha_{\text{red}} = 1$). The function $E(z)$ represents the electrode potential that is equal to the difference between the electronic and ionic potential taken in the Ni and YSZ phase respectively (i.e. $E(z) = \varphi_{\text{el}}(z) - \varphi_{\text{io}}(z)$). Since the reaction takes place at the sites where ions, electrons and gas species meet, the forward kinetic constant, k_{ox} , has been scaled with the density of 'active' TPBs, ζ_{TPB} :

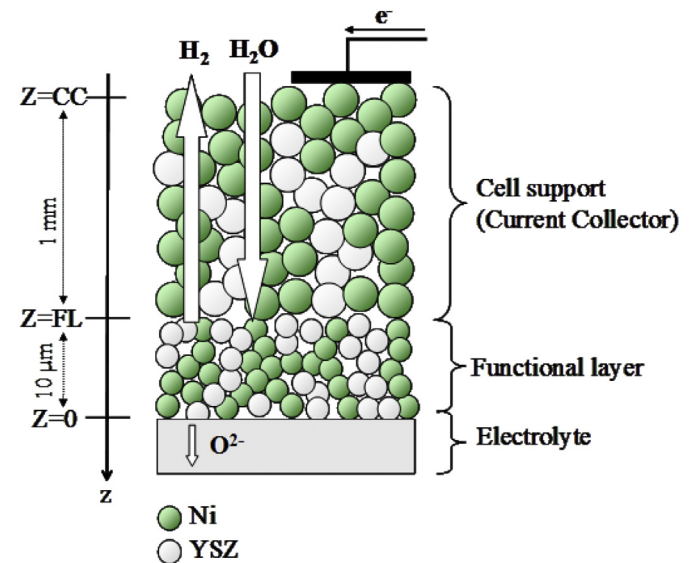


Fig. 3. Electrode geometry considered in the model. The system of coordinate used for the simulation is also represented.

$$k_{\text{ox}} = \zeta_{\text{TPBI}} \times k_0^{\text{ox}} \times e^{-\frac{\Delta H_{\text{ox}}}{RT}} \quad (9)$$

where k_0^{ox} denote the orientation factor and ΔH_{ox} the activation energy for charge transfer. It can be noticed that k_{red} is deduced from the k_{ox} at the Open Circuit Potential (OCP).

For the current collector substrate, it can be observed in Fig. 1b that the structure of Ni, pores and YSZ are connected and continuous through the interface between the functional layer and the cell support. The gas, ions and electrons can flow from one layer to the other. As a consequence, the electrochemical reaction could potentially extend into the bulk of the collector. In order to estimate this possibility, the model described in Ref. [8] has been modified in such way that the electrochemical reaction could occur at the active TPBIs of the substrate. For this purpose, the same set of equations than that used for the functional layer are solved into the cell support. In this case, the model parameters are expressed according to the microstructure properties of the Ni–YSZ substrate.

It can be noticed that the 'apparent' electrode potential \tilde{E} corresponds to the difference of the electronic potential taken at the free surface of the electrode $\varphi_{\text{el}}(z = \text{CC})$ and the ionic potential taken at the electrolyte interface $\varphi_{\text{io}}(z = 0)$:

$$\tilde{E} = \varphi_{\text{el}}(z = \text{CC}) - \varphi_{\text{io}}(z = 0) \quad (10)$$

The global electrode overpotential $\tilde{\eta}$ is then expressed as the subtraction between \tilde{E} and the OCP $E_{i=0}$: $\tilde{\eta} = \tilde{E} - E_{i=0}$. This expression of the global electrode overpotential can be decomposed in two distinct contributions:

$$\begin{aligned} \tilde{\eta} &= \eta^{\text{ohmic}} + \eta^{\text{electrochem}} \\ \text{with } \eta^{\text{ohmic}} &= \{\varphi_{\text{el}}(z = \text{CC}) - \varphi_{\text{el}}(z = z^*)\} \\ \text{and } \eta^{\text{electrochem}} &= \{\varphi_{\text{el}}(z = z^*) - \varphi_{\text{io}}(z = 0)\} - E_{i=0} \end{aligned} \quad (11)$$

where z^* is the position in the electrode for which the electrochemical reaction rates tends to 0. In other words, the distance $d = |z^*|$ corresponds to the thickness of the active layer since it represents the full extent of the reaction from the electrolyte interface. Therefore, the component η^{ohmic} is equal to a pure ohmic contribution ascribed to the electrical resistivity of the inactive part of the Ni–YSZ bilayer; whereas the term $\eta^{\text{electrochem}}$ represents the potential losses including all the phenomena that hindered the reaction itself. It encompasses a combination of the charge transfer, the gas transport up to the TPBIs, and a limitation induced by the ionic and electronic transport within the active layer. This contribution corresponds to the so-called polarisation resistance of the electrode [25].

3. Results and data analysis

3.1. Microstructure quantification

This section of the paper focuses on the determination of the structural parameters from the 3D reconstruction within cathode functional layer and cathode current collector. In order to calculate microstructure properties with reasonable computation times, space resolution has been downsized by increasing the voxel size from 25 to 50 nm (except for the tortuosity factors calculated with a greater voxel size as further discussed). The procedure to decrease the resolution is detailed in Ref. [12].

The CFL reconstructed volume lies just next to the electrolyte and presents a volume of $27.5 \times 27.5 \times 10 \mu\text{m}^3$. It has been subdivided into 9 independent quasi-cubic volume of $9.1 \times 9.1 \times 10 \mu\text{m}^3$ taken as Stochastic Volume Element (SVE) [19,26]. Therefore, the CFL properties values have been averaged on these 9 realizations.

Whereas for the CCC, microstructural parameters have been directly computed from a single volume of $36 \times 36 \times 36 \mu\text{m}^3$, which is slightly larger than the Representative Volume Element (RVE) [12].

3.1.1. Volume fractions, phase connectivity and TPBIs

Volume fraction and connectivity for pore, YSZ and Ni phase as well as TPBIs densities within the CFL and the cathode substrate are summarized in Table 1.

Difference in volume fractions between the two layers is found to be significant as porosity increases from 22.8% within CFL to 46.6 % in the cathode substrate. It can be noticed that the calculated ratio of solid volume fraction Ni/(Ni + YSZ) (0.63 and 0.59 for CFL and cathode substrate, respectively) is in good agreement with the theoretical value given by the manufacturer (0.6 for 50 wt% Ni and 50 wt% 8YSZ). As a consequence, for CFL, 9 SVEs of $9.1 \times 9.1 \times 10 \mu\text{m}^3$ allow obtaining good statistics (and ensure to obtain accurate mean values).

In Fig. 4, the relative error in volume fractions calculated on the CFL has been plotted as a function of the size of sub-domains extracted from the whole reconstruction. It is found that the error becomes negligible for sub-volumes larger than $14 \times 14 \times 10 \mu\text{m}^3$. This volume threshold defines the RVE size which is required to be representative of the CFL fine microstructure. As a comparison, this volume is 22 times lower than the one requested for the coarse microstructure of the cell support.

Both CFL and CCC microstructures present a high level of connectivity. It is greater than 95% for all phases, except for the porosity within CFL which exhibits a lower value of 88%. In Fig. 5, the connectivity has been plotted for the porosity versus the position in the electrode thickness. This curve has been computed for different voxel sizes ranging from 50 to 200 nm. First of all, as expected, it can be noticed that the thickness of the functional layer is approximately equal to 10 μm . Moreover, in the fine microstructure of the functional layer, a voxel size of 100 nm, as a maximum, is necessary to maintain the phase connectivity. Indeed, the pore connectivity is found to be strongly degraded for voxel size superior to 100 nm. In the coarse microstructure of the CCC, the porosity is not affected by the voxel size up to 200 nm. These results indicate that a resolution of 100 nm is required for the CFL while a

Table 1

Volume fractions and connectivity of the phases plus total and active TPBIs calculated for CFL, considering 9 subvolumes of $9.1 \times 9.1 \times 10 \mu\text{m}^3$, and cathode substrate. The standard deviation is calculated for CFL as well as the extremum values. All TPBIs values have been corrected by the coefficient 1/1.455.

	CFL	Cathode substrate
Porosity volume fraction (%)	22.8 min: 20.3, max: 26.5, std. dev.: 2.1	46.6
YSZ volume fraction (%)	49.0 min: 46.2, max: 51.4, std. dev.: 1.7	31.7
Ni volume fraction (%)	28.2 min: 26.7, max: 29.1, std. dev.: 0.8	21.7
Porosity connectivity (%)	88.0 min: 82.7, max: 93.5, std. dev.: 4.3	99.2
YSZ connectivity (%)	99.7 min: 99.6, max: 99.8, std. dev.: 8.2e-2	99.2
Ni connectivity (%)	97.1 min: 95.0, max: 98.9, std. dev.: 1.3	96.7
Total TPBIs (μm^{-2})	4.63 min: 4.42, max: 4.91, std. dev.: 0.16	3.46
Active TPBIs (μm^{-2}) ^a	3.07 min: 2.59, max: 3.42, std. dev.: 0.24	2.61
Active TPBIs (μm^{-2}) ^a	3.30 —	—

^a Active TPBIs calculated on the whole volume (this calculation involves the whole CFL volume and thus the result is more reliable).

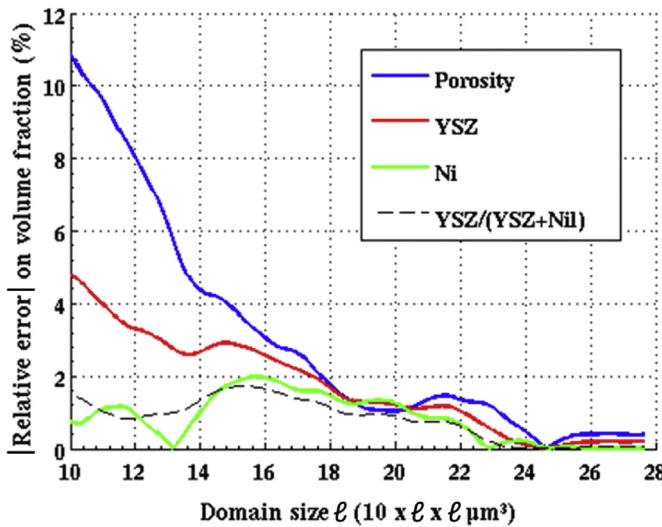


Fig. 4. Relative error in volume fractions plotted as a function of the domain size ℓ (for an analysed volume of $10 \times \ell \times \ell \mu\text{m}^3$ the constant dimension being along the normal axis to the interfaces). Dashed line is the relative error in the ratio of the solid phase $\text{YSZ}/(\text{YSZ} + \text{Ni})$. Volume analysed is extracted from the CFL reconstruction.

resolution of 200 nm is sufficient to describe accurately the connectivity of CCC.

Total and active densities of TPBIs are both reported in Table 1. As already mentioned in Section 2.2, the raw TPBIs are corrected by a coefficient of 1/1.455 because of the discretisation in cubic voxels. As expected, the CFL shows higher active TPBIs density than CCC (i.e. $3.3 \mu\text{m}^{-2}$ for CFL and $2.6 \mu\text{m}^{-2}$ for CCC). It can be remarked that the value of total TPBIs within CFL (i.e. $4.63 \mu\text{m}^{-2}$) is very close to the one given by Joos et al. [27] on the same kind of electrode ($6.79/1.455 = 4.66 \mu\text{m}^{-2}$).

3.1.2. Specific surface area, mean particle size and particle size distribution

Specific surface area, mean particle diameters for pore, YSZ and Ni phases within CFL and cathode substrate are summarized in

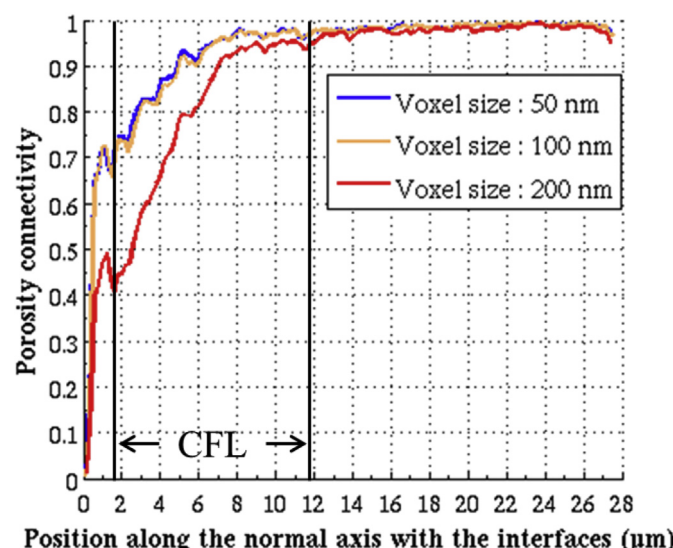


Fig. 5. Porosity connectivity calculated on the whole volume and here plotted on each slice along the normal axis with the interfaces. Data are taken from the CFL reconstruction with a part of the electrolyte on the left. Data has been plotted with different voxel size ranging from 50 to 200 nm.

Table 2. Note that these values have been computed with geometric covariograms and covariance functions (see Section 2.2).

CFL systematically exhibits smaller particles size compared to CCC, as deduced from the covariance functions plotted in Fig. 6. This is especially true for the porosity with a mean particle size of $0.94 \mu\text{m}$ in the functional layer versus $2.6 \mu\text{m}$ in the support. Note that the large difference in porosity size between CFL and CCC can be clearly observed on the 3D reconstruction (Fig. 1). The presence of large pores in the substrate after sintering results in the use of pore-former agents during the manufacturing process [28,29].

Specific surface area for porosity is more than twice within CFL compared to CCC (i.e. 9.09 versus $4.24 \mu\text{m}^{-1}$). This result is in good agreement with the difference in pores diameters between the two layers.

Aside from the method based on geometric covariogram (see Section 2.2), specific surface area has been also computed from a direct analysis of 3D reconstruction. In this case, the specific surface area is calculated by adding all the voxel faces, which are located at the boundary between the phase and the complementary volume [12]. However, this method requires a corrective factor to obtain the real surface since the structure is described by cubic elements. A factor of $2/3$ has been considered in this work that is rigorously applicable only for a sphere described by cubic voxels. In spite of this simplification, specific surface areas computed from the two methods are found to be in good agreement. Indeed, relative error between the two methods is less than 7.5%. As a consequence, the direct method based on the voxel faces summation provides good approximation for SOEC electrode microstructure.

PSDs for CFL and CCC are provided in Fig. 7. It has to be remarked that PSD algorithm gives smaller mean particle diameters than the covariance functions. Indeed, the continuous PSD algorithm used in this work leads to underestimate the real mean particle diameter as already discussed by Holzer et al. [30].

Whatever the electrode layer, histograms of solid phases are quite similar. They present a unimodal distribution with a relative narrow peak. Conversely, two distinct histograms are found for porosity of CFL and CCC. The cathode support exhibits a wide distribution of diameters while the functional layer is centred on a narrow peak. As discussed previously, the wide distribution of pores size in the substrate could be explained by the use of pore-former agents, which should result in large voids after sintering.

3.1.3. Tortuosity factor

A sensitivity analysis has been performed on the tortuosity factor by changing the voxel size. For the functional layer, it has been found that the size of the discretization must be lower than $\leq 100 \text{ nm}$ to compute accurate tortuosities. For the cathode support, the same condition on voxel size is requested for the Ni and YSZ phases ($\leq 100 \text{ nm}$). Regarding the gas phase of the substrate, it has been found that voxels of 200 nm are small enough to compute stable tortuosity factors. It can be remarked that these statements are consistent with the sensitivity analysis performed on phase connectivity. Moreover, a previous study [12] performed on a typical Ni–YSZ support has already shown that a discretisation of 240 nm is sufficient to determine the gas tortuosity factor (with an error lower than 2.5%). Explanation for the dependence of tortuosity factor on voxel size derives from the particle size distributions between the phases. Porosity of the cathode substrate exhibits a non-homogeneous particle size distribution (Fig. 7), that can be simplified with a fine and a coarse pore network. Gas species diffuse mainly through the coarse network of the structure while the fine network has only a limited contribution. The increase in voxel size leads to the removing of a part of the fine network (Fig. 8), resulting to a slight increase in the tortuosity factor. Conversely, the functional layer and the solid phases of the support

Table 2

Specific surface area S_p and mean particle diameter d_{mean} of the phases calculated for CFL, considering 9 subvolumes of $9.1 \times 9.1 \times 10 \mu\text{m}^3$, and cathode substrate. The standard deviation is calculated for CFL as well as the extremum values. The specific surface area has been calculated with the geometric covariogram and the mean particle diameter with the covariance function.

	CFL	Cathode substrate
S_p Porosity (μm^{-1})	9.09 min: 7.88, max: 10.19, std. dev.: 0.81	4.24
S_p YSZ (μm^{-1})	5.50 min: 5.32, max: 5.69, std. dev.: 0.12	6.01
S_p Ni (μm^{-1})	6.54 min: 6.30, max: 6.69, std. dev.: 0.14	5.87
d_{mean} Porosity (μm)	0.94 min: 0.65, max: 1.7, std. dev.: 0.35	2.6
d_{mean} YSZ (μm)	0.73 min: 0.7, max: 0.75, std. dev.: 0.03	1.1
d_{mean} Ni (μm)	0.83 min: 0.75, max: 0.9, std. dev.: 0.06	1.2

present only a fine microstructure (Fig. 7) that has to be described by a higher space resolution.

Since homogenization computations are time consuming, the tortuosity factors have been calculated with a resolution of 100 nm,

except for the porosity of the CCC for which the resolution has been taken to 200 nm. The obtained values along the perpendicular direction to the electrolyte (i.e. z-direction: cf. Fig. 1) are reported in Table 3. Ni and YSZ structure present lower tortuosity factor within CFL than substrate. Since connectivity and PSD are roughly identical between the two layers, that effect could be ascribed to the difference in volume fraction between the two layers.

Unlike the solid phases, porosity exhibits a tremendous increase in tortuosity factor from 2.22 for the substrate to 10.15 for the functional layer. These differences can be explained by both the change in volume fractions and pore size distribution.

3.2. Ni–YSZ electrode modelling

Electrode simulations have been carried out with the microstructural properties determined in the previous section for the Ni–8YSZ bi-layer. The kinetic parameters introduced in the model are provided in Table 4.

3.2.1. Orientation factor k_0^{ox}

For the best knowledge of the authors, there is no value reported in the open literature regarding to the kinetic parameter k_0^{ox} related to a Ni–8YSZ cathode operating in steam electrolysis. As a consequence, the pre-exponential factor k_0^{ox} has been determined in the present study so that the ‘apparent’ exchange current density of the electrode is equal to $i_0 = 537 \text{ mA cm}^{-2}$ at $T = 800 \text{ }^{\circ}\text{C}$. Indeed, this value has been experimentally determined in another study for the same cell that the one studied in this paper [32]. It is reminded that the parameter i_0 is associated to the electrode activation overpotential, which is expressed as follows [5,32]:

$$\eta^{\text{act}} = \frac{RT}{F} \sinh^{-1} \frac{i_{\text{e}^-}}{i_0(T)} \quad (12)$$

The overpotential η^{act} includes all the phenomena that hinder the electrochemical process except the limitation due to the gas transport (that is ascribed to the concentration overpotential [31,32]). The electrode overpotential $\eta^{\text{electrochem}}$, which can be calculated with the electrode model (see eq. (11)), is then equal to the activation overpotential η^{act} only at low current density for which the gas diffusion is not a limiting step [5,33]. As a consequence, the methodology used to estimate k_0^{ox} has been the following: a set of simulations have been carried out at $T = 800 \text{ }^{\circ}\text{C}$ and at low current density (i.e. $|i_{\text{e}^-}| \leq 0.5 \text{ A cm}^{-2}$). The simulations were carried out by changing k_0^{ox} up to obtain a satisfactory adjustment between the electrode overpotentials $\eta^{\text{electrochem}}$ and the activation ones (i.e. η^{act} calculated with eq. (12) by considering an ‘apparent’ exchange current density of 537 mA cm^{-2} [32]). As shown in Fig. 9, the best fit is obtained for $k_0^{\text{ox}} = 29 \text{ mol s}^{-1} \text{ m}^{-1}$. It can be mentioned that, even at the highest investigated current density, the pressure drop across the Ni–8YSZ bilayer remains fairly low meaning that the concentration overpotentials can be neglected (i.e. $\Delta P_{\text{H}_2\text{O}} = 0.02$ at $i_{\text{e}^-} = -0.5 \text{ A cm}^2$). This statement is consistent with previous studies [5,33] that have shown that significant concentration overpotentials arise for typical electrode supported cells only at high current density ($|i_{\text{e}^-}| \geq 1 \text{ A cm}^{-2}$).

3.2.2. Electrode activation energy

Since the electrochemical processes are thermally activated, the ‘apparent’ exchange current density is usually expressed according to an Arrhenius law [5]:

$$i_0(T) = i_{00} \times e^{-\frac{E_a}{RT}} \quad (13)$$

where E_a is the electrode activation energy which is classically employed in a ‘macro’ model developed at the cell or stack level

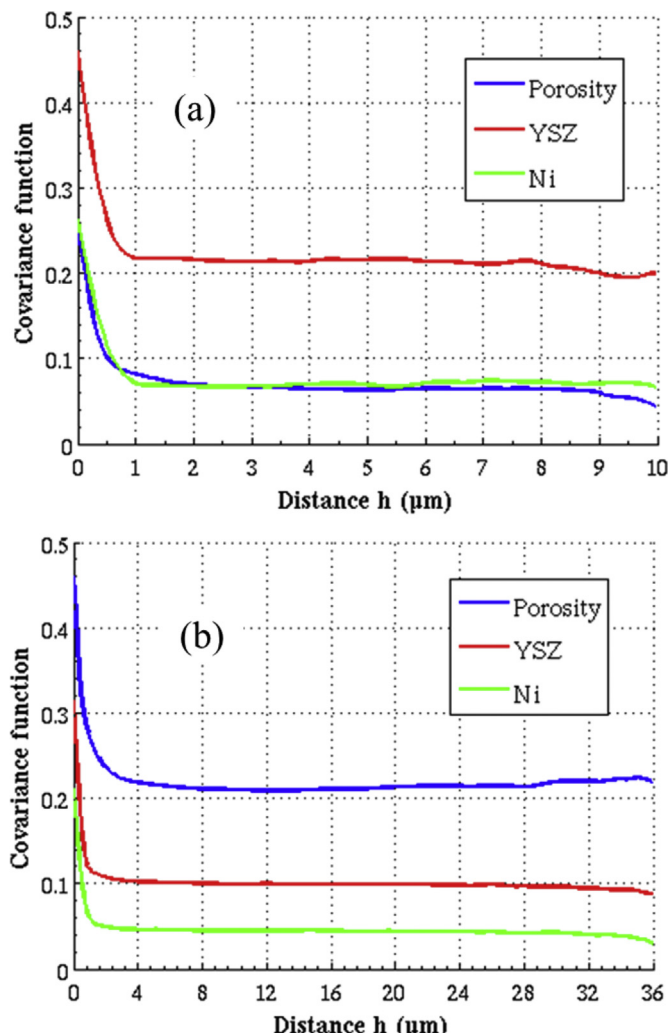


Fig. 6. Covariance function plotted as a function of the distance h calculated (a) on CFL and (b) on the cathode substrate. For the sake of visibility the covariance is plotted only for one subvolume of $9.1 \times 9.1 \times 10 \mu\text{m}^3$ for CFL.

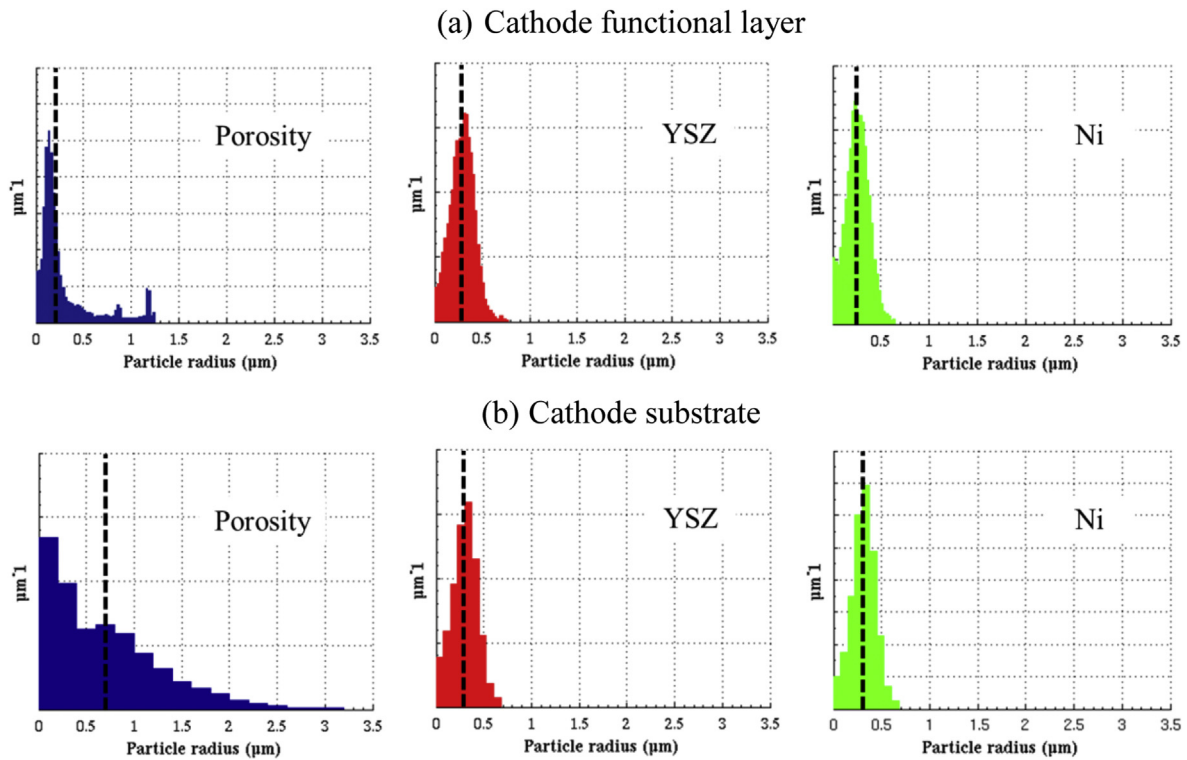


Fig. 7. Particle size distribution (a) on CFL and (b) on the cathode substrate. Voxel size is reduced to $50 \times 50 \times 50 \text{ nm}^3$ in order to describe the smallest spheres within CFL whereas voxel size is increasing to 100 and 200 nm respectively for solid phases and porosity within cathode substrate to get reasonable time calculations. The dashed lines indicate the mean values of the given distribution.

[5,32–34]. Nowadays, despite its great importance, no specific study has been devoted to determine this parameter for a Ni–YSZ cathode.

In order to estimate a reliable value for E_a , the electrode overpotential $\eta^{\text{electrochem}}$ has been computed with the cathode model at $T = 750 \text{ }^\circ\text{C}$ and $T = 850 \text{ }^\circ\text{C}$. As previously mentioned, the calculations are restricted to low current cases to avoid any limitation due to the gas transfer. The simulated cathode overpotential has been then fitted by eqs. (11) and (12) by considering an exchange current density i_0 of 537 mA cm^{-2} at $T = 800 \text{ }^\circ\text{C}$. The fit result is given in Fig. 9. It is found that the dependence on temperature of the electrode overpotentials is accurately described by relations (12) and (13) for an activation energy of $E_a = 120.5 \text{ kJ mol}^{-1}$. This value encompasses the activation energies associated to the thermally activated phenomena controlling the whole electrochemical process. It can be noticed that the value obtained in this study is in good agreement with the reported activation energies by Costamagna and Honegger [35] (i.e. $E_a = 120$ and 140 kJ mol^{-1} for an Ni–YSZ composite operated as SOFC anode under hydrogen at $800 \text{ }^\circ\text{C}$).

At low current density, it can be reasonably expected that the electrode response is mainly governed by the kinetic of the electrochemical reaction and the oxygen ions transport in the YSZ structure of the active layer [8]. Indeed, the contribution of the species depletion along the electrode, or the concentration overpotential, can be neglected in this case. However, this work shows that the electrode activation energy is not a single combination of the activation energies related to the ionic conduction (i.e. 83 kJ mol^{-1}) and charge transfer on Ni–YSZ material (i.e. 201 kJ mol^{-1}). Thanks to a micro model, only the correct description of the reaction delocalization through the functional layer and its microstructure properties is able to supply reliable values of the effective exchange current density.

3.2.3. Thickness of the active layer $d = |z^*|$

Thanks to the present study, the microstructure properties of electrode and its kinetic parameters are known. As a consequence, it becomes possible to assess with the electrode model the real extent of the electrochemical reaction into the Ni–YSZ bilayer. For this purpose, the local volume specific current $j(z)$ has been computed versus the position z in the electrode (Fig. 10). It is reminded that $j(z)$ represents the electrochemical source terms that are produced in the active layer. Indeed, the local specific current $j(z)$ is linked to the kinetic rates of the electrochemical reaction $v(z)$ according to $j(z) = 2F \times v(z)$. As shown in Fig. 10, it is found that source terms $j(z)$ associated to the electrochemical reactions occur in the whole functional layer; whereas the extent of the reactions into the substrate is very limited. This result can be explained by two main reasons:

- Firstly, the decrease of the electrochemical reaction rates is very steep in the depth of the functional layer (Fig. 10). At $10 \mu\text{m}$ from the electrolyte interface, the electrochemical reaction rates start to be limited (they represent only $\approx 5\%$ of the maximum value obtained at the interface with the electrolyte ($z = 0$)). This sharp decrease of the electrochemical reaction is mainly explained by the difficulty of oxygen ions to diffuse over a large distance into the functional layer [8]. It means that, for the studied microstructure, the delocalisation of the electrochemical reaction beyond an active layer of $10 \mu\text{m}$ is very limited.
- The previous phenomenon is reinforced by the poor electrochemical activity of the cell substrate because of its coarse microstructure. Indeed, the concentration of active sites is significantly lower in the cell support in comparison to the functional layer (i.e. $\zeta_{\text{TPBI}}^{\text{cell support}} / \zeta_{\text{TPBI}}^{\text{functional layer}} = 0.8$). Moreover, the oxygen ions mobility through the YSZ structure of

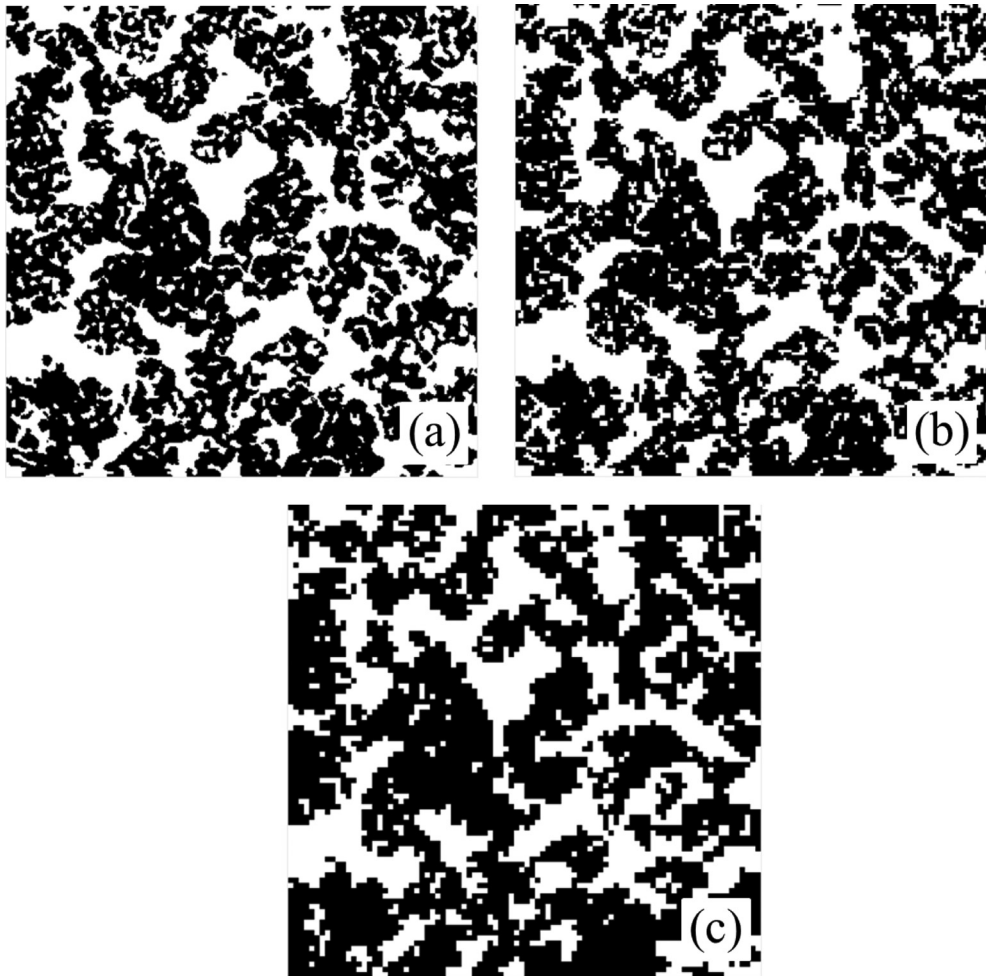


Fig. 8. Bidimensional view extracted from the middle of the cathode substrate reconstruction. White is the percolating porosity phase and black is the complementary volume. Voxel size is (a) $100 \times 100 \times 100 \text{ nm}^3$, (b) $200 \times 200 \times 200 \text{ nm}^3$ and (c) $400 \times 400 \times 400 \text{ nm}^3$. The fine percolating network is preserved with a discretization up to a voxel size of 200 nm whereas it has almost been removed for a voxel size of 400 nm.

Table 3

Tortuosity factor calculated for CFL, considering 9 subvolumes of $9.1 \times 9.1 \times 10 \mu\text{m}^3$, and cathode substrate. The standard deviation is calculated for CFL as well as the extremum values. The tortuosity factor has been calculated along the axis normal to the interfaces. Voxel size is 200 nm for porosity within cathode substrate and 100 nm for all others phases.

	CFL	Cathode substrate
Porosity	10.15 min: 7.26, max: 15.06, std. dev.: 2.88	2.22
YSZ	2.28 min: 1.97, max: 2.88, std. dev.: 0.33	3.63
Ni	5.50 min: 4.40, max: 7.68, std. dev.: 0.99	8.65

Table 4

Kinetic parameters for Ni–YSZ electrode simulations.

Electrode material	Activation energy for charge transfer ΔH_{ox} (J mol $^{-1}$)	Orientation factor k_0^{ox} (mol s $^{-1}$ m $^{-1}$)	Symmetry factor α_c and α_a
Ni-8YSZ	201 \times 103 [31]	29 ^a	0.5

^a Value determined in this study.

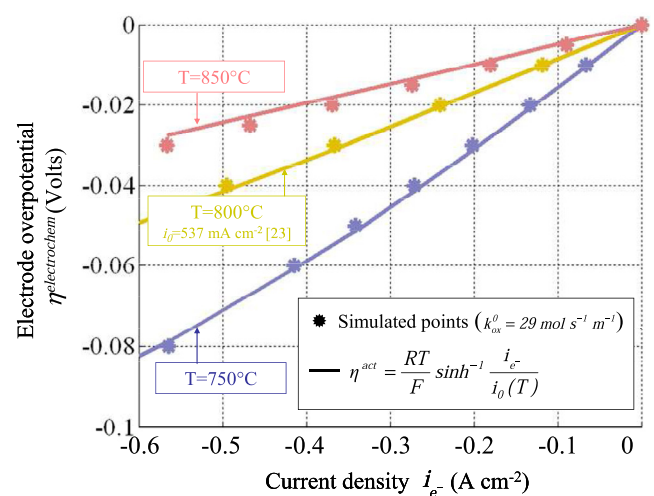


Fig. 9. Electrode overpotential $\eta^{\text{electrochem}}$ simulated for the Ni-8YSZ cathode bi-layer in 10% H₂ and 90% H₂O. The microstructure properties taken for the simulations are provided in Section 3.1. The simulated points are compared to the activation overpotential η^{act} .

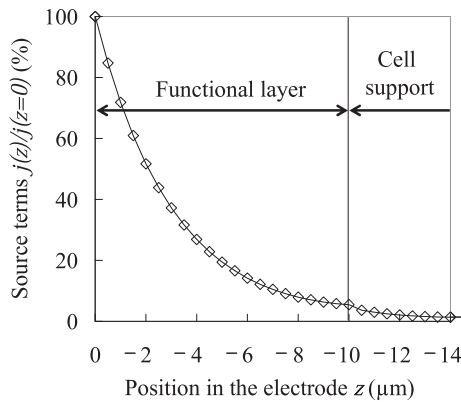


Fig. 10. Delocalization of the electrochemical reaction for the Ni-8YSZ cathode bi-layer in 10% H₂ and 90% H₂O (at $T = 800$ °C for an electrode overpotential of 0.02 V). The microstructure properties taken for the simulations are provided in Section 3.1.

the cell support is very limited. Indeed, the tortuosity factor of this ionic conducting phase in the current collector substrate is much higher than the one related to the functional layer (i.e. $\tau_{\text{YSZ}}^{\text{cell support}}/\tau_{\text{YSZ}}^{\text{functional layer}} = 1.6$).

Therefore, it can be inferred from this analysis that the delocalization of the electrochemical reaction within the cell support is very low meaning that its participation to the electrochemical reactions can be neglected. As a consequence, it can be assumed that the dimension of the active layer can be approximately restricted to the functional layer (i.e. $d = |z^* - \text{FL}|$).

4. Conclusion

Microstructure of a cermet Ni–YSZ bi-layer has been analysed on the basis of 3D reconstructions obtained on both functional layer and cell support. Thanks to the large field of view of the reconstructions (≈ 50 μm), microstructure properties have been quantified with a high level of confidence. Indeed, it has been shown that the analysed volumes are statistically representative of the electrode bi-layer microstructure.

For the first time, all the microstructure properties of gas, ionic and electronic phases have been determined for the studied typical Ni–YSZ cermet. Connectivity of each phase, mean particles diameters, specific surface area, particle size distributions, tortuosity factors and densities of TPBIs have been quantified for both functional layer and cell support.

Microstructure parameters have been introduced in an SOEC cathode micro model that takes into account the specific configuration of the Ni–YSZ composite double-layer. Simulations have shown that the extent of the electrochemical reaction in the support is very limited and can be neglected. The SOEC cathode exchange current density has been computed as a function of temperature. It has been found that the combination of ionic conduction and charge transfer all along the volume of the electrode results in an apparent activation energy of 120.5 kJ mol⁻¹.

Acknowledgements

The authors would like to thank Dr. Pierre Bleuet from CEA-Liten for useful discussions and his valuable support on this work. This study has been partially obtained in the framework of a national program called 'Django' and financed by the French National Research Agency (ANR).

References

- [1] M. Ni, Michael K.H. Leung, Dennis Y.C. Leung, Int. J. Hydrogen Energy 33 (2008) 2337–2354.
- [2] J. Mougin, A. Mansuy, A. Chatroux, G. Gousseau, M. Petitjean, M. Reytier, F. Mauvy, Fuel Cells 13 (4) (2013) 623–630.
- [3] Van N. Nguyen, Q. Fang, U. Packbier, L. Blum, Int. J. Hydrogen Energy 38 (2013) 4281–4290.
- [4] X. Zhang, J.E. O'Brien, R.C. O'Brien, J.J. Hartvigsen, G. Tao, G.K. Housley, Int. J. Hydrogen Energy 38 (2013) 20–28.
- [5] J. Laurencin, D. Kane, G. Delette, J. Deseure, F. Lefebvre-Joud, J. Power Sources 196 (2011) 2080–2093.
- [6] J. Laurencin, F. Lefebvre-Joud, G. Delette, J. Power Sources 177 (2008) 355–368.
- [7] J.W. Kim, A.V. Virkar, K.Z. Fung, K. Metha, S.C. Singhal, J. Electrochem. Soc. 146 (1) (1999) 69–78.
- [8] E. Lay-Grindler, J. Laurencin, G. Delette, J. Aicart, M. Petitjean, L. Dessemond, Int. J. Hydrogen Energy 38 (2013) 6917–6929.
- [9] J. Villanova, J. Laurencin, P. Cloetens, P. Bleuet, G. Delette, H. Suhonen, F. Usseglio-Viretta, J. Power Sources 243 (2013) 841–849.
- [10] R.N. Basu, G. Blass, H.P. Buchkremer, D. Stöver, F. Tietz, E. Wessel, I.C. Vinke, J. Eur. Ceram. Soc. 25 (2005) 463–471.
- [11] P. Cloetens, W. Ludwig, J. Baruchel, D. Van Dyck, J. Van Landuyt, J.P. Guigay, M. Schlenker, Appl. Phys. Lett. 75 (19) (1999) 2912–2914.
- [12] J. Laurencin, R. Quay, G. Delette, H. Suhonen, P. Cloetens, P. Bleuet, J. Power Sources 198 (2012) 182–189.
- [13] N. Epstein, Chem. Eng. Sci. 44 (1989) 777–789.
- [14] O. Lanzi, U. Landau, J. Electrochem. Soc. 137 (2) (1990) 585–593.
- [15] C.F. Berg, Phys. Rev. E 86 (046314) (2012) 1–9.
- [16] L. Holzer, D. Wiedenmann, B. Münch, L. Keller, M. Prestat, Ph. Gasser, I. Robertson, B. Grobety, J. Mater. Sci. 48 (2013) 2934–2952.
- [17] A. Haas, G. Matheron, J. Serra, Ann. Mines XI (Dec. 1967) 736–753 vol. XII, dec. 1967, 768–782.
- [18] S. Torquato, Microstructure and Properties, Interdisciplinary Applied Mathematics, vol. 16, Springer, 2001.
- [19] T. Kanit, S. Forest, I. Galliet, V. Mounoury, D. Jeulin, Int. J. Solids Struct. 40 (2003) 3647–3679.
- [20] L.D. Gelb, K.E. Gubbins, Langmuir 15 (1999) 305–308.
- [21] L. Holzer, B. Iwanschitz, Th. Hocker, B. Münch, M. Prestat, D. Wiedenmann, U. Vogt, P. Holtappels, J. Sfeir, A. Mai, Th. Graule, J. Power Sources 196 (2011) 1279–1294.
- [22] N. Vivet, S. Chupin, E. Estrade, T. Piquero, P.L. Pommier, D. Rochais, E. Bruneton, J. Power Sources 196 (2011) 7541–7549.
- [23] J.R. Wilson, J.S. Cronin, A.T. Duong, S. Rukes, H.-Y. Chen, K. Thornton, D.R. Mumm, S. Barnett, J. Power Sources 195 (2010) 1829–1840.
- [24] A. Weber, E. Ivers-Tiffée, J. Power Sources 127 (2004) 273–283.
- [25] S. Primdahl, M. Mogensen, J. Electrochem. Soc. 144 (1997) 3409–3418.
- [26] G. Delette, J. Laurencin, F. Usseglio-Viretta, J. Villanova, P. Bleuet, E. Lay-Grindler, T. Le Bihan, Int. J. Hydrogen Energy 38 (2013) 12379–12391.
- [27] J. Joos, M. Ender, I. Rotscholl, N.H. Menzler, E. Ivers-Tiffée, J. Power Sources 246 (2014) 819–830.
- [28] N.H. Menzler, F. Tietz, S. Uhlenbruck, H.P. Buchkremer, D. Stöver, J. Mater. Sci. 45 (2010) 3109–3135.
- [29] L. Mingyi, Y. Bo, X. Jingming, C. Jing, Int. J. Hydrogen Energy 35 (2010) 2670–2674.
- [30] L. Holzer, B. Münch, B. Iwanschitz, M. Cantoni, Th. Hocker, Th. Graule, J. Power Sources 196 (2011) 7076–7089.
- [31] Wolfgang G. Bessler, S. Gewies, M. Volger, Electrochim. Acta 53 (2007) 1782–1800.
- [32] J. Aicart, J. Laurencin, M. Petitjean, L. Dessemond, Fuel Cells (2014) (in press).
- [33] J. Udagawa, P. Aguiar, N.P. Brandon, J. Power Sources 166 (2007) 127–136.
- [34] M. Ni, J. Power Sources 202 (2012) 209–216.
- [35] P. Costamagna, K. Honegger, J. Electrochem. Soc. 145 (1998) 3995–4007.